Post-disaster Damage Assessment of Bridge Systems

FINAL REPORT
August 2022

Submitted By:

Xiao Liang

Assistant Professor

University at Buffalo

212 Ketter Hall, Buffalo, NY 14260

Seyed Omid Sajedi

Research Assistant

University at Buffalo

212 Ketter Hall, Buffalo, NY 14260

External Project Manager:

Christopher LaTuso
NY/NJ Transportation Program Manager
HDR, Inc.

In cooperation with

Rutgers, The State University of New Jersey
And
U.S. Department of Transportation
Federal Highway Administration

Disclaimer Statement

1. Report No. CAIT-UTC-REG 50	2. Government Accession No.	3. Recipient's Catalog No.
4. Title and Subtitle Post-disaster Damage Assessment of Bridge Systems		5. Report Date August 2022
		6. Performing Organization Code CAIT/University at Buffalo
7. Author(s) Xiao Liang https://orcid.org/0000-0003-4788-8759 Seyed Omid Sajedi https://orcid.org/0000-0002-4552-4794		8. Performing Organization Report No. CAIT-UTC-REG 50
9. Performing Organization Name and Address University at Buffalo 212 Ketter Hall, Buffalo, NY 14260		10. Work Unit No.
		11. Contract or Grant No. 69A3551847102
12. Sponsoring Agency Name and Address Center for Advanced Infrastructure and Transportation Rutgers, The State University of New Jersey 100 Brett Road Piscataway, NJ 08854		13. Type of Report and Period Covered Final Report 2/1/2021-7/31/2022
		14. Sponsoring Agency Code
15. Supplementary Notes U.S. Department of Transportation/OST-R 1200 New Jersey Avenue, SE Washington, DC 20590-0001		

16. Abstract

The existing ML models for vibration-based damage assessments often use highly compressed features or are restricted to preprocessed signals with fixed durations and sampling rates. Additionally, the learning capacities of ML models and computational resources are limited, which restricts using raw signals as direct input. This report studies Mel Filter Banks (MFBs) for seismic signal processing, inspired by speech recognition technology. It is argued that the same filter designs in audio engineering may not be appropriate for seismic records, and therefore, customized filter bank formulation is developed. Hybrid Deep learning models for Rapid Assessments (HyDRA) are introduced as multi-branch neural network architectures that enable end-to-end training for different types of processed vibration data structures. Moreover, the performance-based earthquake engineering (PBEE) equation is adjusted to integrate ML model uncertainties for probabilistic assessments. The proposed concepts are validated in a case study based on a dataset of 32,400 nonlinear time history analyses on a highway bridge in California. Insights and guidelines are provided for optimum filter design based on 5,184 experiments. Several HyDRA architectures are compared with benchmark models. It is shown that the optimized MFB feature type outperforms features obtained from continuous wavelet transform and a stacked vector of conventional earthquake engineering indices. Finally, a Bayesian variant of HyDRA is investigated to showcase its integration in the modified PBEE equation. Adopting custom filter banks with the HyDRA architecture enables effective feature extraction from raw vibration records by diversifying feature space and preserving information in the time and frequency domains.

17. Key Words Signal processing, Hybrid deep learning; Mel filter banks; Seismic damage diagnosis; Vibration-based assessments; Structural Health Monitoring		18. Distribution Statement	
19. Security Classification (of this report) Unclassified	20. Security Classification (of this page) Unclassified	21. No. of Pages 53	22. Price

Form DOT F 1700.7 (8-69)

Acknowledgments

Table of contents

List of figures

List of tables

Chapter 1: Introduction

The 2021 Report Card for America's Infrastructure identified that 42% of the nation's bridges are more than 50 years old, and 7.5% are considered to have "poor" conditions (ASCE 2021). If appropriately designed, Machine Learning (ML) models can provide valuable information for stakeholders and decision-makers regarding civil infrastructure repair, maintenance, and safety assessments. They can ultimately contribute to saving millions of dollars in infrastructure maintenance and repair costs by providing timely condition assessments. Structural health monitoring (SHM), especially vibration-based damage diagnosis, is one of the areas where ML can be a powerful tool. Moreover, federal programs such as the USGS's National Strong Motion Project (NSMP) imply that the number of instrumented structures is rising, and ground motion data is available within minutes following seismic events (CESMD 2021; Haddadi et al. 2012).

Processing sensor data in (near) real-time is essential for rapid structural assessments after extreme events. Nevertheless, this task is associated with several challenges, especially for ML models. Time series associated with ground motions (GM) events have different durations and are not often recorded with unique sampling rates. Most classical ML algorithms cannot adapt to these data sizes and resolution variabilities as they accept fixed-size inputs. How raw signals can be used in model training is one of the most significant design challenges in data-driven SHM.

Xu et al. (2021) have attempted feeding raw ground motions (GMs) to long short-term memory (LSTM) neural networks for regional seismic assessments by preprocessing the data to

match sampling rates and window durations. The one and two-dimensional convolutional neural networks are also utilized by reshaping vibration records into one or two-dimensional representations (Abdeljaber et al. 2018; Khodabandehlou et al. 2019; Eltouny and Liang 2022). However, the data for both cases were obtained under controlled laboratory experiments without variabilities that are often observed when using existing ground motion datasets.

Acceleration records are often recorded in thousands of time steps, making training robust ML models computationally demanding. Manual feature engineering is another area where some studies have focused on finding damage-sensitive features from vibration records. Many of these works rely on the rich history of structural and earthquake engineering research for feature extraction (Avci et al. 2021; Guan et al. 2021). A review of the latest work in this domain is provided in what follows. Muin et al. (2020) investigated several manual features, including peak acceleration, cumulative absolute velocity (CAV), and spectral accelerations (Sa), as the input to their novelty detection model. Liang et al. (2018), Sajedi and Liang (2020), and Eltouny and Liang (2021) extended the definition of CAV to I^η and constructed a vector of I^η scalers for both the ground motion and the building response. Furthermore, it was shown that these compressed representations could be used in larger sensor arrays where features are fed as a tensor with multiple channels to a fully convolutional neural network (Sajedi and Liang 2020b). Mangalathu and Jeon (2020) utilized the continuous wavelet transform of ground motions. To classify earthquake damage, they treated processed vibration data like images and fine-tuned computer vision models such as ResNet and VGG-16. Azimi and Pekcan (2020) preprocessed the time series by data compression in the form of histograms and further extracted the mean, standard deviation, and scale parameters to represent a signal. While manually engineered features can be indicators

of structural damage, some information is inevitably lost due to signal preprocessing transformations, especially when time series are compressed into a scalar representative.

Inspired by human speech recognition technology, this report investigates deep vibration-based damage detection utilizing Mel Filter Banks (MFB). Human speech (e.g., pronouncing a word or a sentence) is often recorded as a time series. Both representations contain thousands of time steps despite the inherent physical differences between structural vibrations and human speech signals (e.g., accelerations vs. acoustics). Audio signals are often recorded with resolutions in kHz, while the existing ground motion records often used in structural response history analyses rarely exceed 1 kHz. With that said, a similar approach that can deal with lengthy and high-resolution audio signals can also benefit vibration-based seismic damage diagnosis systems. Moreover, representing signals in the frequency domain has been a powerful tool in earthquake engineering for applications such as conditional ground motion generation (Tamhidi et al. 2021), which is also conceptually implemented in MFBs.

Automatic speech recognition (ASR) is one of the areas where the latest advances of AI and deep learning have played a pivotal role. In addition to sophisticated deep learning architecture designs, utilizing MFBs is critical in successful ASR frameworks (Chan et al. 2016). The early works of Davis and Mermelstein (1980) built the foundation of signal preprocessing by proposing Mel Frequency Cepstral Coefficients (MFCC). Interestingly, the word cepstrum (the spectrum of the log of the spectrum of a time waveform) was initially used by Bogert et al. (1963) to identify echoes in seismic signals (Oppenheim and Schafer 2004).

Few studies in the literature have investigated the application of such features for structural and earthquake engineering. For example, algorithms based on Squared Mahalanobis Distance (SMD) have been used for anomaly detection by comparing the MFCC representation of damaged and undamaged structures (Balsamo et al. 2014; Civera et al. 2019; Ferraris et al. 2020). Mei et al. (2019) performed principal component analysis on MFCCs. They compared the features in different damage states, and Dackermann et al. (2014) utilized cepstral analysis for damage detection in an ensemble of neural networks on a laboratory scale test specimen.

This report investigates the original Mel scale and filter banks and customizes this formulation for optimal performance in ML models for earthquake and structural engineering applications. While MFBs are a rich source of information for vibration-based SHM, manually engineered features from other signal processing techniques can also benefit prediction accuracy. Hybrid Deep learning models for Rapid Assessments (HyDRA) are introduced in this report as a type of deep learning algorithm that can integrate different sources of processed seismic data in a single neural network architecture with end-to-end training. Finally, the original performance-based earthquake engineering (PBEE) equation is modified to integrate the deep learning model's uncertainty.

Chapter 2: Filter Banks

Due to variations in the human ear's critical bandwidth, lower frequencies often contain more important information about phonetically important speech characteristics (Davis and Mermelstein 1980). For this reason, the Mel scale is formulated to discretize the frequency range into increments that are closely spaced increments at lower frequencies. Arguably, the same logic may not apply to seismic signals. To better investigate the differences between different frequency scales, the original equation that relates Hz and Mel is generalized as follows:

$$m_c = \kappa \log(1 + \frac{f}{\alpha}) \tag{1}$$

$$f = \alpha(10^{m_c/\kappa} - 1) \tag{2}$$

where f and mc respectively correspond to frequencies in Hz and the custom Mel scale. By substituting $\kappa = 2595$, and $\alpha = 700$, the original Mel scale can be obtained from Hz and vice versa. These two constants are based on studies on frequency ranges that the human ear can perceive. For the applications proposed in this report, κ has no significance and will be eliminated in the calculation explained later. For simplicity, the following equations will assume $\kappa = 1$. Nonetheless, the appropriate selection of α is crucial, and its significance is better understood by examining how filters are built. Note that from this point forward, when referring to MFB or MFCC, it will be implied that custom scaling is used rather than the original implementation.

The signal sampling rate (SR) must be determined to acquire the filters. The frequency range for the signals is then considered as the range between $f^l = 0$ and f^u where the upper

bound f_h is often set to SR/2 Hz based on the Nyquist theorem. With that said, the bounds of the frequency range can be converted to the corresponding custom Mel frequencies where $m_c^l = 0$ and:

$$m_c^u = \log(1 + \frac{SR}{2\alpha}) \tag{3}$$

The next step in obtaining the filters is uniformly discretizing the frequency range $[m_c^l, m_c^u]$ into the desired number of filters (N_f). After obtaining each frequency increment, they are converted back to Hz. Given that the selected bounds of frequency in Hz are not a function of κ , as stated earlier, its value does not affect the filters. Davis and Mermelstein (1980) initially proposed 20 triangular bandpass filters used in deep learning ASR models. For a variety of reasons, the same filter design may not be adequate for assessing structural vibrations. The spacing of filters is not only affected by α but also SR. Audio signals are often recorded in sampling rates of 44.1 kHz and above (AES 2018). Our initial inspection of 180 ground motion records indicated that the strong ground motion records commonly used in seismic response history analyses rarely exceed 1kHz (0.001s time steps). As a result, the nonlinearly spaced filters for audio signal processing will be approximately equally spaced, assuming $\alpha = 700$ and $SR < 1\,\mathrm{kHz}$. Figures 1.a and 1.b help illustrate these differences.

Moreover, a different choice of filter shape might yield better results for seismic applications. To further investigate the proper design of filters, a new hyperparameter $0 \le \beta \le 1$ is introduced in this report. β is the y-intercept of the line that passes through (SR/4, 1) as shown in Figure 1.c. Increasing β from a default of 0 will put more emphasis on higher frequencies. Moreover, a rectangular filter shape will be investigated as an alternative.
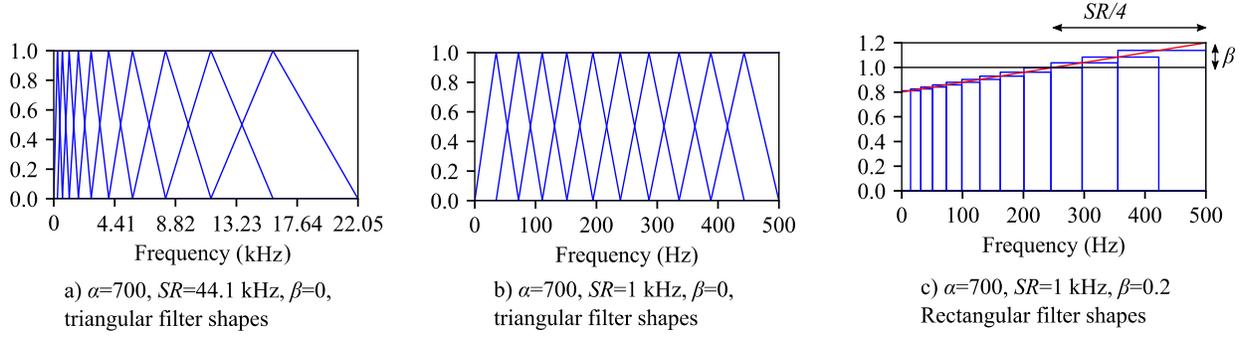
Figure 1. Variation in filter designs for earthquake engineering vs. human speech recognition

Once the filters are constructed, MFBs can be calculated. The objective of filter banks is to indicate how much energy is stored in different frequency bins. Therefore, the waveform is transformed into a periodogram using the Fast Fourier Transform (FFT). Element-wise multiplication of each filter to the periodogram results in a vector with values that indicate the amount of energy stored in each frequency bin. It is theoretically possible to calculate filter banks on a complete signal. However, the waveform is evaluated individually by a series of shorter and overlapping windows with a size of t_w, which helps to monitor the temporal variations of the signal as well as frequency. By doing so, a single-channel vibration record will be preprocessed into a 2D tensor denoted as MFB.

When constructing the filters, the selection of hyperparameters should not result in computationally invalid filters. These issues can appear when the frequency resolution of a signal's periodogram is lower than the filters. Hence, some filters will contain zero information while occupying memory (Figure 2). The first frequency increment after the lower bound, f^1, should be less than or equal to the frequency increment of the periodogram (f^p) to avoid this conflict. The two can be expressed as follows:

$$f^1 = \alpha(10^{dm} - 1) \tag{4}$$

$$f^p = \frac{SR}{2N_{FFT}} \tag{5}$$

where N_{FFT} is the number of FFT points and dm is the constant distance between frequency increments in custom Mel scale and can be obtained by Eq. 6:

$$dm = \frac{m_c^u - m_c^l}{N_f + 2} = \frac{\log\left(1 + \frac{SR}{2\alpha}\right)}{N_f + 2} \tag{6}$$

To satisfy $f^p < f^1$ and by replacing dm in Eq. 4, the minimum value of N_{FFT} to avoid this numerical issue can be obtained by satisfying:

$$N_{FFT} \geq \frac{SR}{2\alpha\left(\sqrt[N_f+2]{1 + \frac{SR}{2\alpha}} - 1\right)} \tag{7}$$

The maximum value of N_{FFT} should be selected concerning the number of time steps in each time window.

Since time windows are often highly correlated in speech signals, another step is often taken by performing a discrete cosine transform in the time dimension. This new feature is known as MFCC. MFB and MFCC for a 2D representation have identical tensor shapes. Later in the study, we will examine whether MFCCs outperform MFBs in seismic damage detection, just as they do in human speech recognition. Additionally, some insights will be provided on the selection of α, β, N_f, N_{FFT}, and t_w.
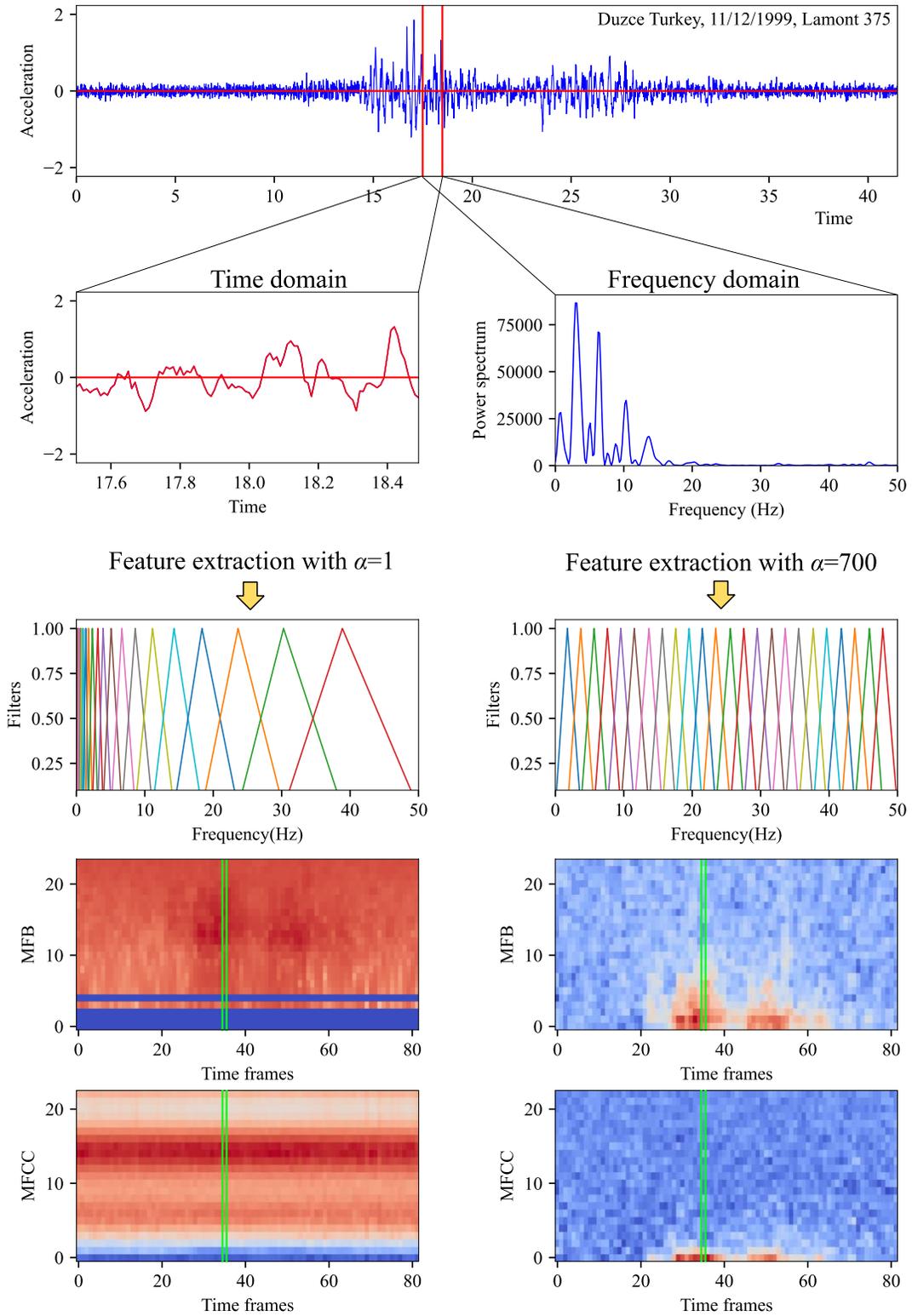
Figure 2. Extraction of MFB and MFCC for different values of α. The solid bands in the left

MFB tensor contain empty filter banks caused by inappropriate hyperparameter selection.

Chapter 3: Hybrid Deep Learning

Deep learning algorithms are capable of constructing highly nonlinear relationships between input-output pairs in noisy real-world observations. Regardless of the learning capacity of these advanced and trending models, one should be aware of their limitations. While ML models can automatically learn abstract features from data, the learning algorithm has not yet evolved to the extent of eliminating the need for domain expertise in feature extraction. Note that this limitation is different from the computational demands of training ML models for raw signals. Even with hypothetically unlimited computational resources, the existing neural network models cannot ideally learn the physical concepts as the human brain does. Given these limitations in the learning algorithm, neural network models are often prone to overfitting or cannot provide perfect predictions without integrating domain expertise from structural engineering. In this case, one can hypothesize that an ML model will be more robust if trained with several diverse sources of processed information in an end-to-end fashion. To better understand this versatility in input information, one might consider the following example. One can hypothesize that an ML model for seismic damage detection can be more robust if, in addition to feature extraction from raw signals, it is also equipped with earthquake engineering metrics that are correlated with structural damage.

We propose Hybrid Deep learning models for Rapid Assessments (HyDRA) to show that it is possible to combine different sources of information such as sequential MFB representations and more conventional earthquake engineering indices like PGA, CAV, I^{η}. HyDRA begins with different branches. Each branch has a network head comprised of a neural network architecture

designed for appropriate feature extraction of its corresponding engineered features (EF). For example, MFBs include temporal variations of a signal, and a recurrent neural network (RNN) head might suit this branch. Moreover, RNNs can process and learn from variable-length input sequences, which is a great advantage for this data type. Each network head will output a set of abstract learned features (ALF) concatenated with other ALFs from different network heads. Simpler EFs such as single scalar indexes (e.g., PGA) can be directly concatenated with other ALFs without requiring a network head. After concatenation, the combined features are passed to a bottleneck for a final prediction. Figure 1 illustrates a generic HyDRA model that is enabled for end-to-end training.
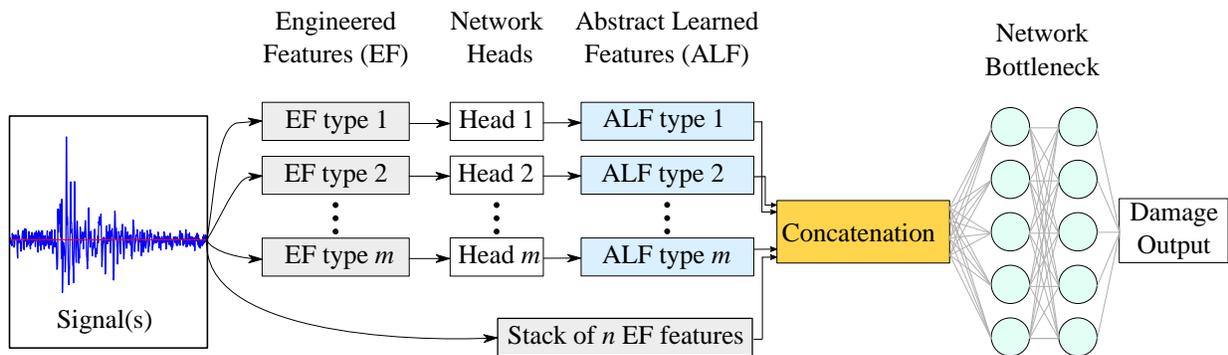
Figure 3. HyDRA model description

The above description of HyDRA implies how flexible and generalized this architecture can be. This flexibility can be approached from different perspectives. Different network heads can each be designed with a customized architecture depending on the application and data availability. It is recommended to use a neural network bottleneck for initial training and calibrating the network heads to generate damage-sensitive ALFs. A typical HyDRA model will automatically learn to construct mappings between different sources of input (EFs), and optimizing the learnable parameters in network heads is part of this process. Once this task is complete, it is

possible to discard the bottleneck portion of HyDRA and use it as a feature extractor instead of a regression/classification model. As a result, ALFs can be used as the input of other types of ML algorithms, such as XGBoost (Chen and Guestrin 2016), for regression/classification tasks. This report will utilize the neural network bottleneck because the model uncertainty can be effectively quantified with Monte Carlo dropout sampling (Gal and Ghahramani 2016). In the case study section of this report, we will discuss and compare several possible HyDRA configurations for seismic damage assessments.

Chapter 4: Performance-based Assessments

The performance-based earthquake engineering (PBEE) philosophy divides seismic loss assessments into logical steps where different uncertainties can be studied and taken into account. With that said, the following equation initially presented by Cornell and Krawinkler (2000) is probably the basis of modern PBEE (Hamburger et al. 2012):

$$\lambda(DV) = \int_{DM} \int_{EDP} \int_{IM} G(DV \mid DM) dG(DM \mid EDP) dG(EDP \mid IM) d\lambda(IM) \qquad (8)$$

where DV, DM, EDP, and IM are the decision variable (e.g., earthquake loss), damage measure (e.g., collapse), engineering demand parameter, and intensity measure. Note that $\lambda(x)$ corresponds to the mean annual rate of exceeding an event and $G(x)$ is the complementary cumulative probability distribution function. The proposed methodology in this report is intended to be used for rapid seismic damage assessments and health monitoring. It is safe to assume that uncertainties in vibration records from a seismic event that has already happened can be ignored. In particular circumstances, one might consider factors related to instrumentation like sensors generating corrupted data, noise, etc., in uncertainty quantification of seismic signal.

Variations in ML model prediction are an additional source of uncertainty that is not present in conventional vibration-based assessments. Deep learning models include a substantial number of learnable parameters (W) that are calibrated by training sensor data (S). Therefore, the predicted output, EDP, can be treated as non-deterministic by quantifying $G(EDP \mid \mathbf{W}, \mathbf{S})$. Interested readers may refer to Sajedi and Liang (2021) for further details on the model uncertainty in deep vibration-based SHM. Eq. 8 can be adjusted as follows to integrate the fundamental concepts of PBEE in ML-based SHM:

$$E(DV) = \int_{DM} \int_{EDP} \int_{IM} G(DV \mid DM) dG(DM \mid EDP) dG(EDP \mid \mathbf{W}, \mathbf{S}) d\mathbf{W} \qquad (9)$$

where $E(DV)$ is the expected value of the decision variable based on vibration input S due to a seismic event. The calculations regarding $G(DV \mid DM)$ in Eq. 9 may require insights from stakeholders and domain expertise in PBEE. Details of such calculations are not within the scope of this study. Documents and resources from FEMA-58 provide insights for the evaluation of loss (ATC 2012). Regarding $G(EDP \mid \mathbf{W}, \mathbf{S})$ and $G(DM \mid EDP)$, the case studies will be presented in the next section with details on how to quantify the HyDRA's EDP output uncertainty and subsequently use that information for fragility-based labeling.

Chapter 5: Case Study

5.1 Finite Element Model

A single pier reinforced concrete bridge in Ripon, California, is adopted to validate the proposed concepts in this report. The bridge has two spans of approximately 33 m and was built in 2001. The finite element (FE) modeling and seismic performance of this bridge are thoroughly studied by Kaviani et al. (2014). The backfill joints and shear key behaviors are modeled with nonlinear springs. Moreover, the bridge pier utilizes a nonlinear fiber section model. The bridge column drifts are considered as the EDP and to construct the probability distribution corresponding to $G(DM \mid EDP)$. We utilize the strain-based limit states proposed by Caltrans, also used by Muin et al. (2020) for ML-based damage diagnosis. The bridge column's fiber section is clustered into different regions, and seven strain-based limit states (LS 1-7) are considered, as shown in Fig 4.

LS-1: Cover cracking ($\varepsilon_t > 1.32 \times 10^{-4}$)
Any outermost cover fiber

LS-2: Minor cover spalling ($\varepsilon_c > 0.005$)
Any outermost cover fiber

LS-3: Major cover spalling ($\varepsilon_c > 0.005$)
Any cover fiber between 1/2-3/4 cover depth

LS-4: Exposed core ($\varepsilon_c > 0.005$)
Any innermost cover fiber

LS-5: Core shedding ($\varepsilon_{cu} > 0.025$)
Any outermost core fiber

LS-6: Rebar rupture ($\varepsilon_{su} > 0.1$)
Any rebar

LS-7: Near collapse ($\varepsilon_{cu} > 0.025$)
Average core fibers at 1/4 of the core depth

Core concrete   Cover concrete

Figure 4. Strain-based limit states and fiber clusters

5.2 Ground Motion Selection

180 bidirectional GMs are selected from the PEER NGA-West2 online database by considering an M7 earthquake scenario (Ancheta et al. 2014). Specific details regarding the size hazard characteristics are similar to Sajedi and Liang (2020a). GMs are highly variable in terms of recorded duration and sampling rates. These variations are demonstrated in Figure 5. Signal sampling rates range from 50-416.7 Hz, corresponding to 0.02-0.0024s record time steps.
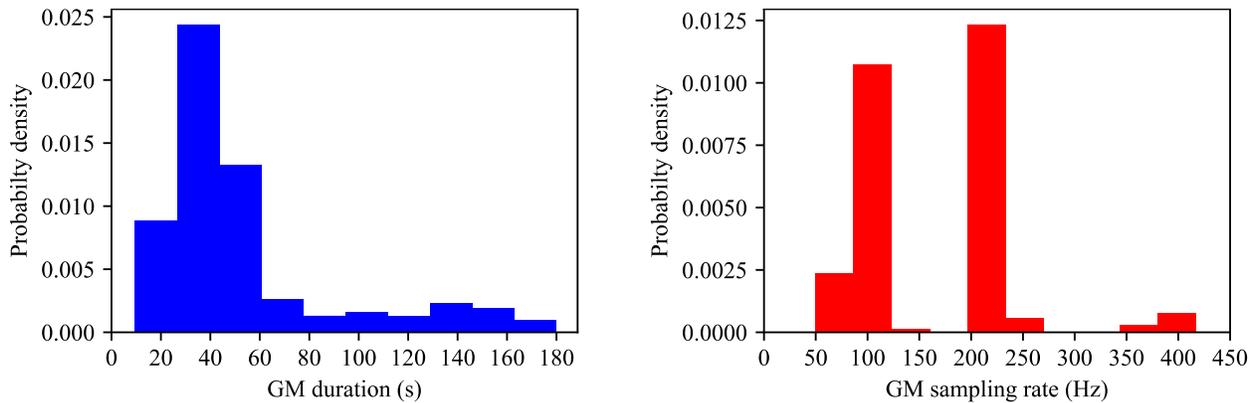
Figure 5. GM duration and sampling rate variations

Several studies have shown that peak ground velocity (PGV) correlates well with seismic structural damage (Akkar and Özen 2005; Küçükdogan 2007; Riddell 2007), and therefore, 30 different intensity measures are considered for each ground motion record. The scaling factors are sampled from the PGV probability distribution using the CB-2014 GM attenuation model (Campbell and Bozorgnia 2014) with a similar approach suggested by Liang and Mosalam (2020). Furthermore, six different intercept angles with 30° increments are considered. The dataset is generated by performing 32,400 nonlinear response history analyses (Liang et al. 2016) using OpenSees and considering all possible combinations (McKenna et al. 2010). The observations with

transient peak column drift greater than 7.5% are later removed, resulting in 32,209 data points. We select this drift limit based on the experimental work conducted by Dutta (1999) to ensure the deformations from FE analyses are in acceptable ranges.

The raw input vibration data for the proposed models in this report is obtained from accelerations in two horizontal directions for the base (GM) and top of the bridge column (structural response) for the duration of an event (tg). All signals are artificially distorted with white Gaussian noise and consider a noise to signal variance ratio of 20%. Time series are subsequently transformed into the MFB or MFCC representation. The 2D processed feature tensors in the two horizontal directions at the top column node are subtracted from the corresponding features in the base column node. The subtracted features in each direction are vertically stacked, forming a single sequence of filter banks with twice the filter banks of an MFB or MFCC obtained from each sensor channel. This process is illustrated in Figure 6.

Bearing pad and stemwall

Shear key

$MFB_{top,X}$

$MFB_{top,Y}$

$MFB_{bot,X}$

Backfill &
expansion joint

$MFB_{bot,Y}$

Subtraction

H2

Y   Z   X

Intercept angle

Bidirectional
ground motion

H1

Vertical stacking

$MFB_{top,Y} - MFB_{bot,Y}$

$MFB_{top,X} - MFB_{bot,X}$

Input tensor
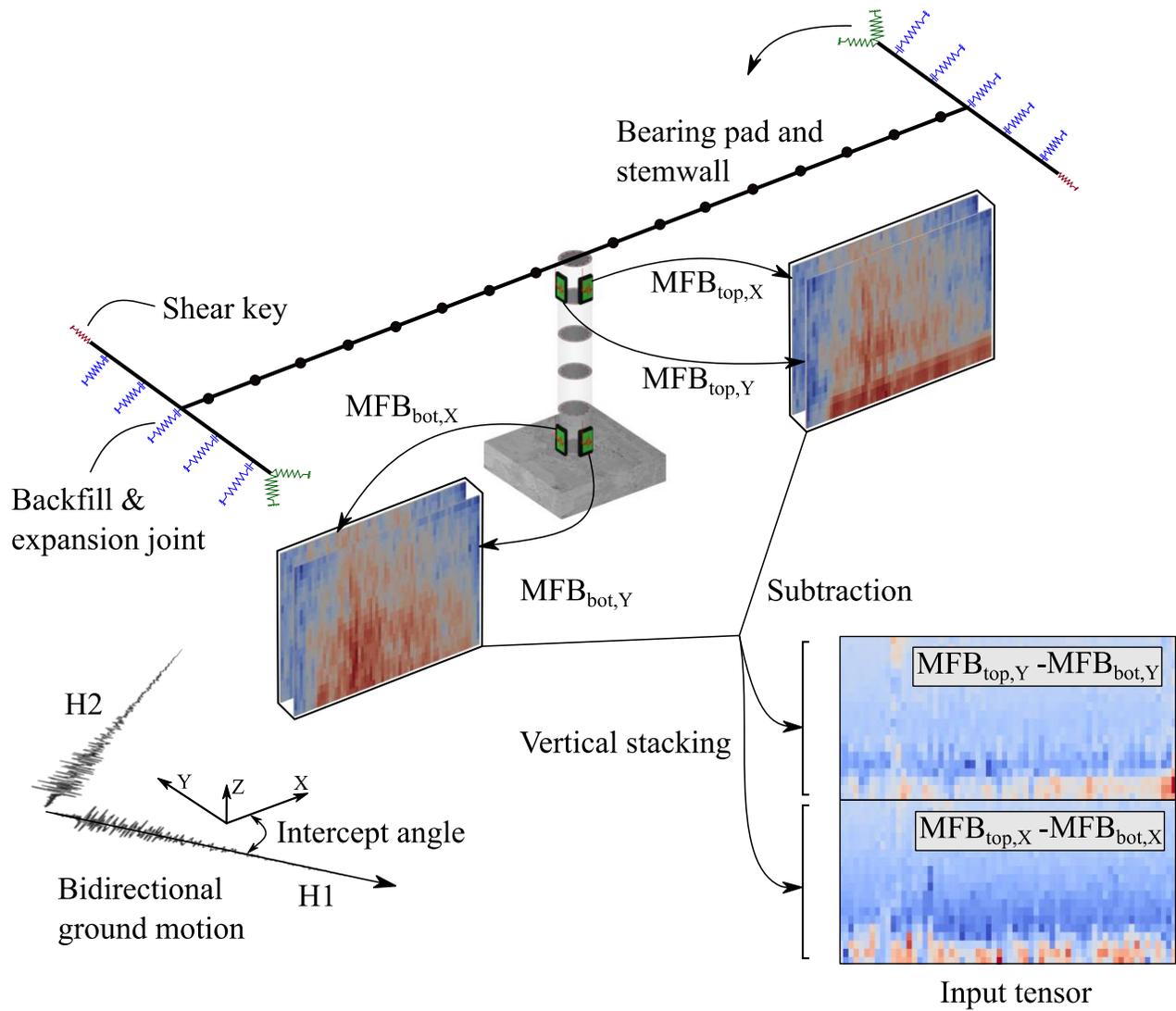
Figure 6. Description of the FEM model and vibration signal processing

Chapter 6: Feature Selection and Filter Design

6.1 Experiment Design

It was previously mentioned that obtaining MFB and MFCC is associated with several hyperparameters optimized for human speech recognition rather than seismic damage diagnosis. The numerical experiment in this section is designed to provide insights and guidelines on the proper selection of hyperparameters α, β, N_f, N_{FFT}, and t_w. Table 1 presents the possible values for these hyperparameters considered in this experiment.

Table 1. Hyperparameter search space

Hyperparameter	Possible values
α	α_{min}, α_{mid}, 700
β	0, 0.2, 0.5
Range of filters (N_f)	1-12 (12), 1-24 (24),13-24 (24), 1-36 (36), 13-36 (36), 25-36 (24)
N_{FFT} (t_w)	512 (1s), 1024 (2s)
Filter shape	Triangle, Rectangle
Feature type	MFB, MFCC
Ignore the first filter	Logical argument (True or False)

Two window sizes of 1s and 2s are selected. Based on the maximum value of SR in the GM bin, N_{FFT} is selected as 512 and 1024, which is slightly greater than the maximum possible number of time steps in each time window. The possible number of filters (N_f) is set to 12, 24, and 36. Some studies on using MFCC for ASR only keep a portion of filter banks. This study also considers six possible combinations by keeping a specific range of filters, as shown in Table 1. Moreover, the initial investigations show that the magnitude of the first filter bank is relatively

26

larger than the others for most time frames. The effect of ignoring the first filter is also investigated in feature extraction. Three distinct values are considered for α, assuming an upper bound of 700, a lower bound determined based on Eq. 7, and an intermediate value α_{mid}. α_{mid} is obtained by taking the average of uniform filter spacing in the custom Mel scale, assuming the two bounds of α. Lastly, it is also essential to investigate if post-processing MFB into MFCC offers any advantage.

Previous assumptions regarding hyperparameter search space result in 864 unique combinations. The 180 GMs are randomly divided into an 80-20% split. While keeping the 20% test set unchanged, 6-Fold cross-validation is performed to obtain training and validation sets. Note that for a GM in each data split, all possible intercept angles and intensities are considered. A simplified version of HyDRA is used to design filters and evaluate the effect of different hyperparameters (Figure 7). This model is trained independently for 5,184 possible folds and input hyperparameters.

Combined MFCC/MFB Input → Masking → GRU(300) → GRU(50) → Dense(50) → ReLU → Dense(500) → Tanh → Dense(1) → ReLU → Drift
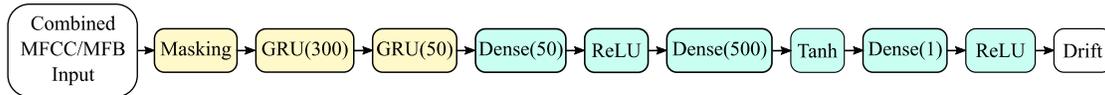
Figure 7. The deep learning architecture used for sensitivity analyses. The value inside parentheses indicates the number of output units. GRU(300) will pass processed features for all time frames to the next layer. GRU(50) will pass the extracted features from the last time frame to the Dense(50).

This simplified model is designed by evaluating a pool of several candidates. In designing this HyDRA variation, both computational efficiency and accuracy are taken into account. All

HyDRA designs are enabled with Masking layers at network heads that enable inputting variable-length processed seismic records directly into the model. Masking will eliminate the need to run all FE simulations for the longest GM or record the vibration response for a fixed duration. This will also accelerate the training and inference time by ignoring the padded frames in each batch.

Gated Recurrent Unit (GRU) layers (Cho et al. 2014) yields slightly better results in our experiments when dealing with sequential seismic data. Moreover, increasing the output dimension of GRUs is more effective than having a stack of multiple GRU layers. For the bottleneck of the network, a combination of ReLU and Tanh activation functions boosted both the accuracy and numerical stability of the model. Nadam Optimizer is utilized along with L1L2 regularization for kernel and biases. For further numerical stability, all drift values are scaled by division to a maximum drift of 0.075. It is also discovered that an 8% dropout for the first GRU layer could slightly improve the model's performance.

6.2 Sensitivity Analyses

This part discusses the proper selection of filters and features based on the validation set's mean absolute error (MAE) metric. The reported MAEs are an average of 6 folds for 864 feature sets. The test MAE is also provided for further reference but is not used as a selection criterion. The MFB settings for the top ten filter designs are given in Table 2.

Table 2. Hyperparameter settings for the top 10 models with the lowest validation MAE

ID.	Val. MAE ($\times 10^{-3}$)	Test MAE ($\times 10^{-3}$)	Filter shape	β	α	N_f	t_w (s)	N_{fk}[b]	1st filter[a]	Type
1	3.921	4.390	Rec	0.0	700	24	2	24	F	MFB
2	3.927	4.442	Tri	0.5	700	24	2	24	F	MFB
3	3.928	4.406	Rec	0.2	700	24	2	24	F	MFB
4	3.954	4.343	Tri	0.0	700	24	2	24	F	MFB
5	3.959	4.400	Rec	0.5	700	24	2	24	F	MFB
6	3.973	4.184	Tri	0.2	700	24	2	23	T	MFB
7	4.009	4.396	Tri	0.2	700	24	2	24	F	MFB
8	4.032	4.332	Tri	0.0	700	24	2	23	T	MFB
9	4.039	4.561	Rec	0.5	700	36	2	24	F	MFB
10	4.047	4.325	Rec	0.5	700	24	2	23	T	MFB

[a] This column denotes whether the first filter is ignored (True or False)

[b] The number of filters out of N_f that are kept are expressed as N_{fk}

The settings used for the remainder of the HyDRA models in this report are from the best-performing model in Table 2. It is also worthy to see how the model performs concerning different hyperparameters. To this end, 50 best and 50 worst-performing cases are also investigated. The bar charts in Figure 8 are divided into two categories of best and worst-performing, and the frequency of distinct hyperparameter values are provided for each category. These graphs show that the model is not sensitive to β, and the default value of 0 will be appropriate. Both filter shapes of triangular and rectangular seem to be performing well. However, rectangular and triangular filter shapes are higher, respectively, in the best and worst-performing settings. MFB is superior to MFCC in all top 10 models. This evaluation shows that 24 is the optimal number of filters, achieving good performance in all 24 cases, and there is no significant gain in ignoring the first filter. It is also evident that setting N_{FFT} (t_w) to 1,024 (2s) results in superior performance as all top 50 models have a 2s window size.
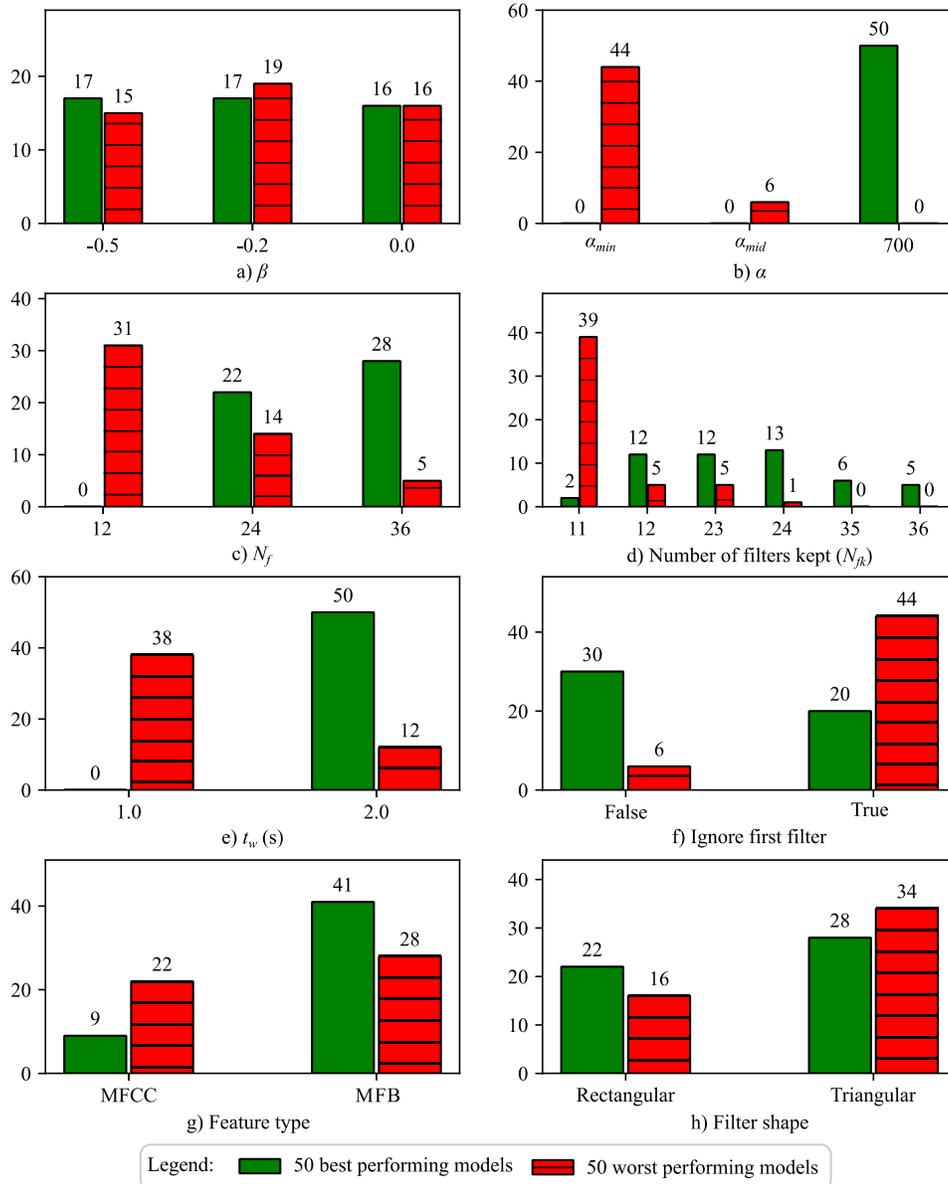
Figure 8. Frequency bar plots comparing the frequency of different hyperparameter selections in the best and worst 50 models based on validation mean absolute error (MAE)

Probably the most important observation from these sensitivity analyses is the spacing of filters based on α. Uniform spacing between the filters works better for this seismic application (i.e., α=700). The higher performance of uniform filter spacings is better observed in Figure 9.

One can hypothesize that this phenomenon is due to two reasons. First, seismic signals and human speech are different physical waveforms, especially considering the sampling frequency. Second, the bin of GM includes variable sampling rates for different observations. It is possible that the nonlinear variable spacing between filters makes the learning process more challenging because signals of different sampling rates are present in the dataset.
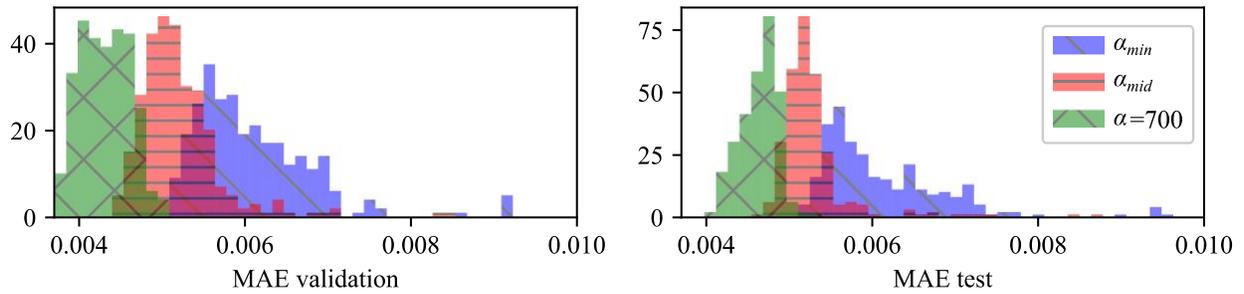
Figure 9. Histogram of validation and test MAE for different filter spacings based on α

Chapter 7: Multiheaded Network Architectures

HyDRA is proposed as a model that enables end-to-end training by combining different EFs. While enriching the feature space can result in more robust predictions, this framework also helps conduct a series of comparative studies for the importance of different EFs. MFB is a single type of EF investigated in the previous section as the network head corresponding to this feature will be referred to as M from this point forward. Inspired by the existing literature, we consider two other benchmark EFs that result in a total of 3 possible network heads and, therefore, 7 neural network architectures (Figure. 10). Details on the two benchmark EFs and their network heads are given in what follows.

Mangalathu and Jeon (2020) have used Continuous Wavelet Transform (CWT) for vibration-based seismic damage diagnosis. CWT is based on mathematically different concepts compared to MFBs, yet the data structure for both feature types is similar (time vs. frequency). It should be noted that this work is different from several perspectives. For example, the mentioned methodology treats CWT output as an image and utilizes deep learning computer vision models (e.g., Liang 2019). HyDRA architectures are based on recurrent neural network architectures that learn from temporal variations in data. The models in this report are custom-designed and trained from scratch on a substantial number of seismic events and tailored for damage diagnosis. Regardless of these differences, a comparison between the two EFs is desired. To this end, the input of the second HyDRA branch is obtained by CWT on acceleration channels. The Morse basis function is adopted as the wavelet basis function to be consistent with Mangalathu and Jeon (2020). The CWT input tensors are further resized with average pooling resulting in 1s time frames and

24 frequency coefficients for each sensor channel. These assumptions are used to obtain relatively close CWT and MFB tensor sizes for a better comparison. The same subtraction and vertical stacking techniques used for MFBs are considered to combine CWT output from different sensor channels. This feature tensor will be the first benchmark EF, and its corresponding network head will be denoted as W. The W branch is identical to M in terms of architecture, as shown in Figure10.h.

Muin et al. (2020) studied several scaler index EFs for data-driven vibration-based damage diagnosis. Inspired by this study and the authors' previous work on cumulative intensity measures (Sajedi and Liang 2020a), the second benchmark EF is a stacked input vector of scalar indices. This vector includes the ground motion duration (t_g), SR, and peak acceleration (PA) for each sensor channel. Four R^{η} features assuming $\eta \in \{0.4, 0.8, 1.2, 1.6\}$, as the ratio of I^{η} values in the bottom and top column nodes in each direction is also appended to the previous feature vector. Details regarding the implementation of R^{η} can be found in Sajedi and Liang (2020b). This stacked vector of scaler features will be the second benchmark EF, and the corresponding branch will be detonated as Z. It is possible to include a multilayer perceptron before these stacked vectors similar to the MFB and CWT feature. For simplicity, these features are directly fed to the network bottleneck.

Each branch will produce a set of ALFs concatenated in the pipeline before the multilayer perceptron in the bottleneck. The notations B and C correspond to the network bottleneck and the concatenation operator. Compared with the architecture shown in Figure.7, in the network bottleneck, everything is similar except that the first dense layer has 500 output units instead of

50. This modification accommodates the extra feature size due to concatenation. Depending on EFs and the corresponding branches used in each HyDRA architecture, MW, MZ, WZ, and MWZ models and a single M are compared with benchmark W, and Z. Detailed architecture of each component can be found in Figure 10.h.
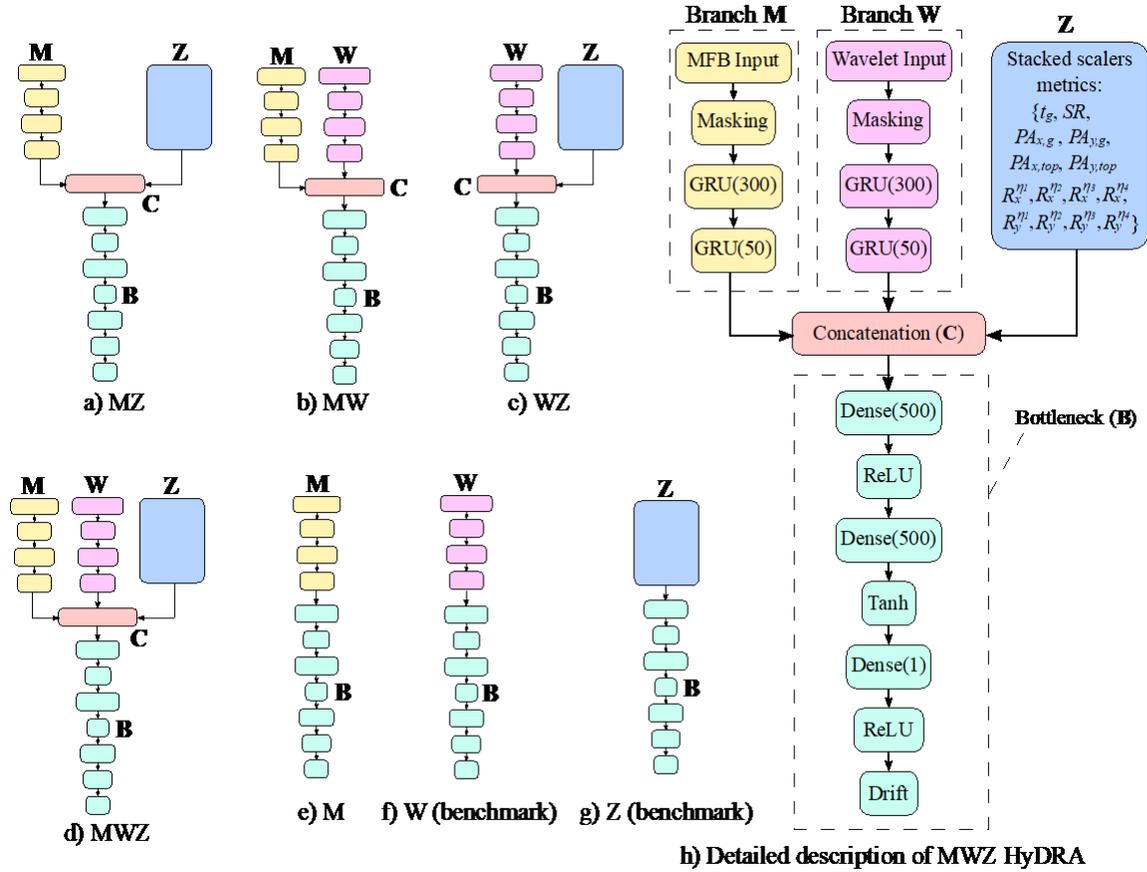
Figure 10. HyDRA architecture designs with different input branches.

Four training sessions are conducted with different weight initializations, and the model with the lowest validation loss is chosen for evaluating the test performance. Test and validation MAEs of each model are illustrated in Figure 11.a. This scatter plot illustrates that all candidates equipped with MFB (M, MW, ZW, MZW) outperform the benchmarks in drift regression accuracy.

It is also discovered that the ensemble model that averages the predictions of each fold results in better performance (Figure 11.b). Moreover, features containing temporal variations of frequency (M, W) yielded better performance than Z.

Later in the report, we will integrate the HyDRA in the PBEE formulation. To this end, the Bayesian version of the best-performing model (MZW) is also included in the performance metrics. The only difference between the standard and Bayesian versions of MZW is the use of dropout after the Dense(500) layers in the network's bottleneck. Bayesian inference takes the expected values of a model's prediction after drawing T Monte Carlo dropout samples. The improvement in results is insignificant when using T=50 instead of 20, while the inference time is almost doubled. This HyDRA design is also used for the next section, where the model uncertainty output is required. A detailed summary of test performance for all HyDRA variants discussed previously can be found in Table 3.

Table 3. Test MAE (×10-3) for different HyDRA variants

| Fold | Benchmarks | | | | | | MZW | | |
	M	W	Z	MZ	MW	ZW	Standard	Bayesian $(T=20)$	Bayesian $(T=50)$
1	4.000	5.818	6.263	4.091	4.163	5.213	3.979	3.996	3.991
2	4.174	5.301	5.961	3.993	4.197	5.213	3.879	3.994	3.990
3	3.975	5.397	5.816	4.219	4.208	5.296	4.064	4.045	4.045
4	4.069	5.286	6.026	4.031	4.196	5.242	3.960	3.897	3.906
5	4.118	5.557	6.032	4.213	4.035	5.083	4.275	4.038	4.044
6	4.168	5.142	6.549	4.104	4.628	5.107	4.188	3.967	3.958
Average[a]	4.084	5.417	6.108	4.109	4.238	5.192	4.058	3.990	3.989
Ensemble[b]	3.792	4.984	5.922	3.800	3.861	4.789	3.761	3.675	3.673

[a]Average MAE error with respect to different folds

^(b)Ensemble MAE is obtained by comparing the ground truth with the average predictions of different folds
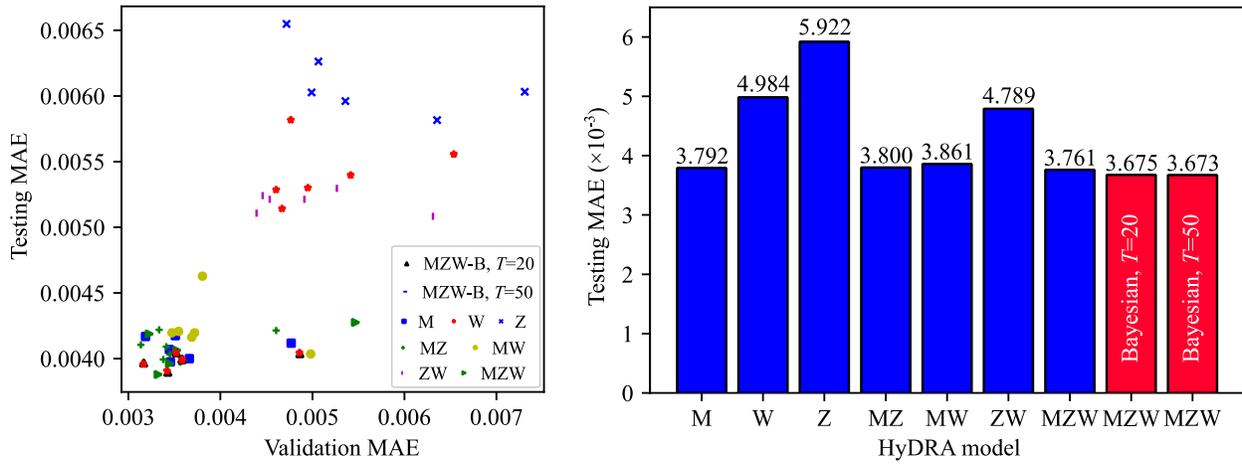
Figure 11. Test performance of 7 HyDRA variants and the ensemble models.

Chapter 8: Fragility Analyses

In this section, we briefly showcase how $G(EDP | \mathbf{W}, \mathbf{S})$ and $G(DM | EDP)$ in Eq. 9 can be estimated. While taking the expected values from a Monte Carlo dropout sample, the standard deviation can be used as a measure to estimate the deep vibration-based model uncertainty (Sajedi and Liang 2021a,b, Sajedi et al. 2022). To this end, the processed seismic input is repeatedly fed to the Hydra Model while a random set of network parameters is activated each time. Dropout layers with 50% probability are placed after the Dense layers. This hyperparameter design adequately captured the HyDRA model's uncertainty. It is also discovered that by combining the samples from the models trained for each fold, a more reliable estimate of the model uncertainty is obtained considering the more diverse and larger sample size that considers the difference in each fold's training data distributions. Figure 12 presents a scatter plot of the Bayesian MZW (T=50) in which expected predictions vs. the ground truth are illustrated. The predictions are sorted in magnitude, and uncertainty contours are obtained by different coefficients of standard deviation from the mean drift predictions. It can be observed that the model uncertainty increases with larger drifts which are expected since the structural behavior will be more complex in more significant nonlinear deformations.

The next step is to estimate the probability distribution of $G(DM | EDP)$. To this end, the large simulation bin obtained from the previous incremental dynamic analyses (IDA) is used. The following procedure briefly describes how fragility curves are extracted for performance-based labeling and loss estimation. Despite differences in some concepts, this implementation is highly inspired by the methodology and mathematical derivations from Baker (2015). It was mentioned

earlier that the strain-based limit states are considered in this report. Therefore, pairs of (strain, peak drift) are sorted based on the peak drift values to construct an IDA line for each ground motion event. We considered 144 training ground motions in 6 different intercept angles, resulting in 864 IDA lines. The scatter plots of (strain, peak drift) values are demonstrated in Figure 13.

The parameter Di needs to be interpolated by finding the smallest drift value that interests the ith IDA line. However, m IDA lines may exceed the maximum drift of 7.5% (Dcap). Additionally, q IDA lines might never reach the limits for both Dcap and the strain associated with the limit state. The values of m and q depend on the data distribution and the severity of damage states. Assuming that the fragility curves follow a lognormal distribution, maximizing the likelihood function can help estimate $\hat{\theta}, \hat{\beta}$, as the two parameters of a smoot fragility curve:

$$\left\{\hat{\theta},\hat{\beta}\right\} = \arg\max \sum_{i=1}^{m} \left\{ \ln\phi\left(\frac{\ln(D_i/\theta)}{\beta}\right) \right\} + (n-m-q)\ln\left(1-\Phi\left(\ln\frac{\ln\left(D_{cap}/\theta\right)}{\beta}\right)\right) \quad (10)$$

where ϕ and Φ are PDF and CDF of the standard normal distribution, and n is the total number of IDA lines. The BFGS algorithm from the SciPy python library (Virtanen et al. 2020) is used to numerically estimate $\hat{\theta}, \hat{\beta}$. The fragility curves corresponding to different limit states can be found in Figure 13.h.
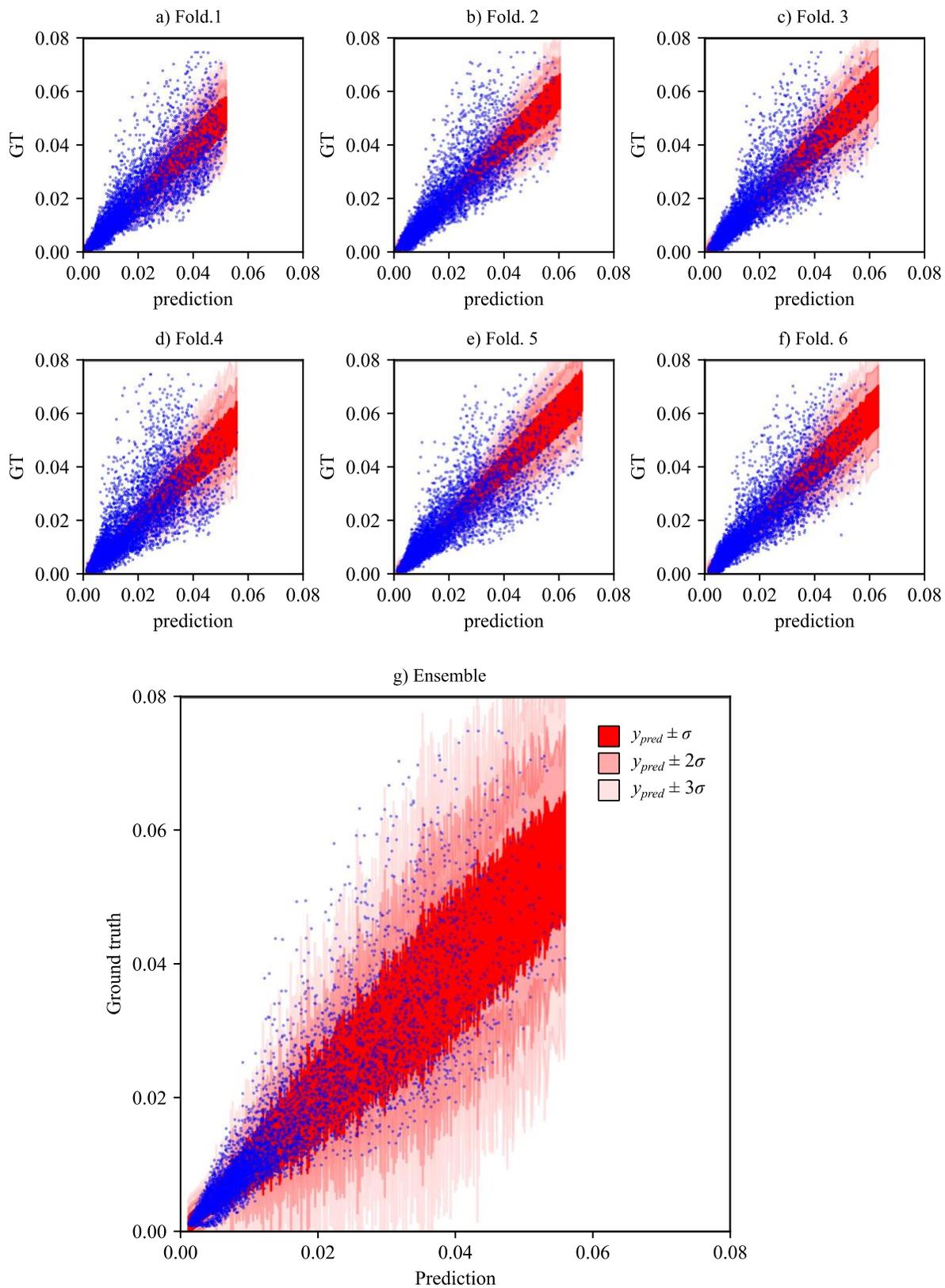
Figure 12. Bayesian XYZ HyDRA (T=50) model uncertainty quantification
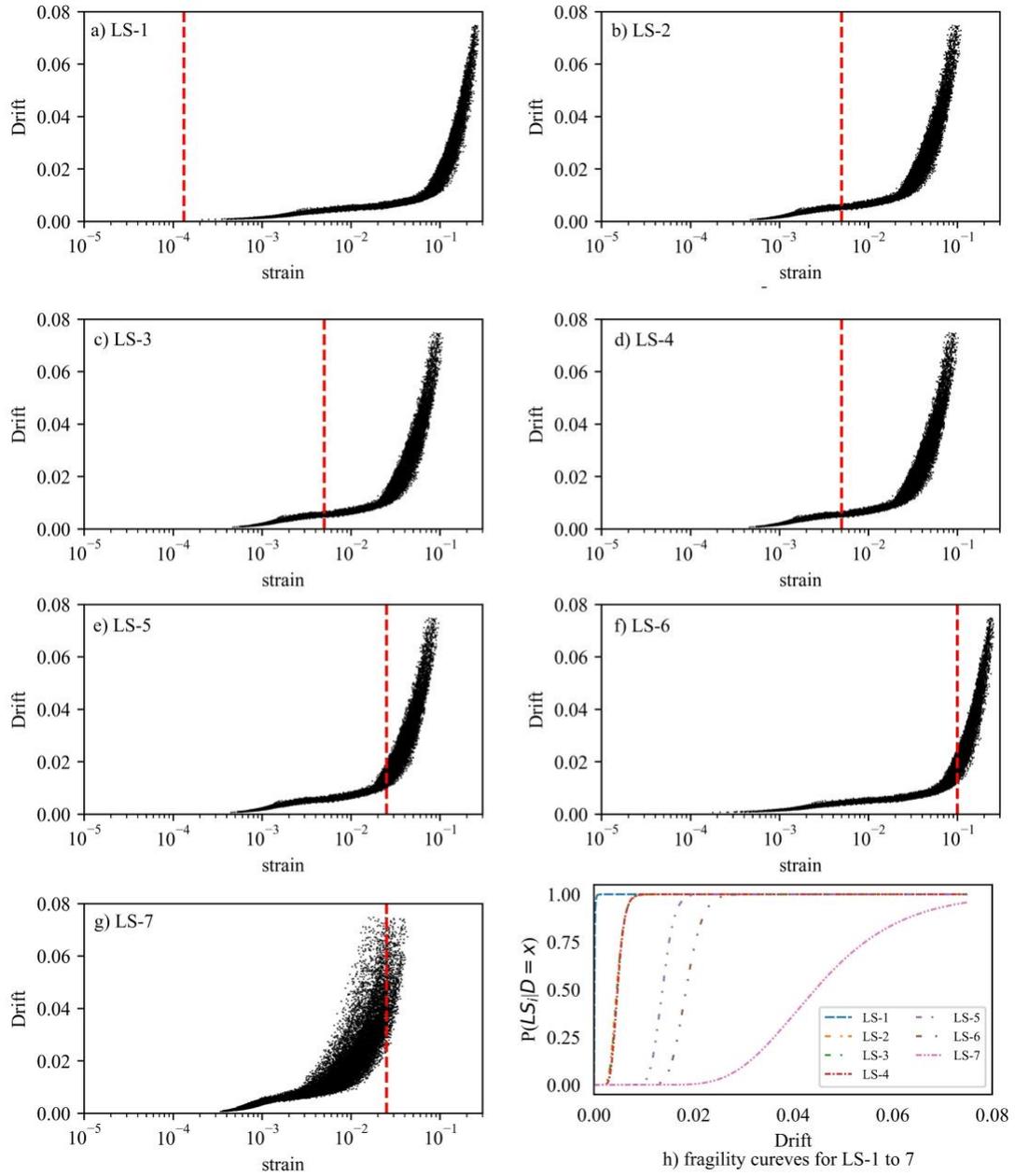
Figure 13. Scatter plots for different strain-based limit states and the corresponding fragility curves

The deep learning model's uncertainty and fragility curves can be used in different ways. A user can obtain the probabilities of different damage states by directly using the drift output of the ML model and reason about the probabilities of different limit states using the fragility curves. Since the output of the HyDRA is associated with uncertainty, this uncertainty can be propagated to the calculation of $G(DM \mid EDP)$ by performing global Monte Carlo sampling, considering the uncertainty of all terms in Eq. 9. Upon the availability of probabilistic models for loss estimation, one can further propagate the deep model's uncertainty in Eq. 9. In this way, a more reliable estimate of the expected DVs (e.g., financial losses) can be obtained.

Chapter 9: Compute Times

The feature selection and filter design simulations are conducted on clusters at the University at Buffalo's Center for Computational Research (UB-CCR). This cloud computing service was especially helpful in conducting parallel FE analyses and further preprocessing the raw vibrations into MFB and MFCC features for 32,209 nonlinear seismic response simulations. The deep learning models are built-in python using Keras deep learning library (Chollet et al. 2015). Multiheaded HyDRA architectures are trained on a personal workstation equipped with an NVIDIA Titan V GPU with 12 GB memory and an Intel Core i9-10980XE CPU.

GM events have different durations, and inference times can vary depending on the sequence length. Furthermore, training convergence and early stopping are not the same for different models depending on weight initialization and random shuffling of batches. Each model is trained and evaluated multiple times on different folds and random initializations to consider these variations. The average and standard deviation required to complete each task and the number of network parameters are given in Table 4. It is observed that once a model is trained, it can process thousands of seismic input tensors in a matter of seconds which can aid rapid damage assessments and post-disaster decision making.

Table 4. Computational details of conducting training and inference in HyDRA architectures

Model	# Parameters	Training and validation duration (min) 25920 events, batch size = 100		Test set inference duration (sec) 6480 events, batch size = 2000	
		Avg.	Std.	Avg.	Std.
M	664301	8.25	2.24	4.03	0.24
W	664301	11.16	2.34	3.95	0.07
Z	258501	1.45	0.62	0.09	0.01
MW	1037101	22.23	8.38	7.85	0.17
MZ	651301	9.10	2.68	3.96	0.06
WZ	651301	11.17	3.02	4.24	0.10
MWZ	1044101	48.42	18.71	8.24	0.26

Chapter 10: Conclusion

Changes in vibration patterns can be indicators of structural damage after seismic events. Finding mappings between vibration data and the extent of damage can be challenging due to nonlinear structural behavior. Machine and deep learning algorithms can be practical tools for interpreting vibration data and rapidly assessing structural damage. The existing machine learning frameworks for vibration-based damage detection often rely on manual feature extractions from signals based on the existing knowledge on scaler indicates that can correlate with damage (PGA, CAV, ..). While these features can be helpful, such manual feature extraction techniques often result in the loss of information because they transform time series data into highly compressed representations. From a different perspective, feeding raw vibration data to ML models is challenging due to the limitations in learning algorithms and the computational costs of training such models. This report tries to address the previous limitations by offering solutions in two different stages.

The first solution is a novel feature extraction technique for deep vibration-based SHM. Inspired by speech recognition technology, custom Mel filter banks (MFBs) are investigated. It shows that the default filter parameters and feature extraction techniques used in audio engineering cannot yield optimal performance for seismic signal processing due to substantial differences in sampling rates and the physical nature of data types. The original formulation of MFBs is modified by introducing several new hyperparameters, including α, β, N_f, N_{FFT}, and t_w, and filter shapes, that enable MFBs to be customized for seismic damage assessments. The second solution is concerned with the design of deep learning architecture. This report develops a multiheaded neural network architecture called HyDRA to learn from different vibration data types with end-

to-end training. A significant advantage of this architecture is that variable length GMs with different sampling rates can be used without further preprocessing or running all GM simulations for extended free vibration periods to achieve fixed-size compatible inputs. The final contribution of this report is that the original PBEE formulation is adjusted to incorporate the deep learning model uncertainty in loss estimations with Bayesian variants of HyDRA.

An RC highway bridge in California is considered as a case study in this report. 32,400 nonlinear response history analyses are conducted on 180 GMs with 6 intercept angles and 30 PGV intensities. The vibration data is used to predict bridge column drifts due to seismic events. A simplified model is initially evaluated for 5,184 different filter bank designs and feature extraction strategies to present insights on selecting filters that maximize seismic performance. More advanced HyDRA architectures are investigated that compared MFB features with benchmark CWT features and a stack of scaler indices, including peak accelerations and R^η. The numerical experiments show that models equipped with MFB outperform the benchmark models. Furthermore, the model that combines all three features yields the lowest MAE in 6-Fold validation and test sets. Lastly, it shows how uncertainty quantification in ML-based predictions and fragility analysis can be integrated into the modified PBEE equation.

This report proposes the concept of customized filter banks for vibration signal preprocessing in ML-based damage diagnoses. Future work is required to study the potential of using other techniques such as Hilbert Vibration Decomposition (HVD) or Empirical Mode Decomposition instead of FFT to extract features in the frequency domain and build filter banks accordingly. Subtraction and stacking techniques also have limited capabilities to handle effective

learning from large sensor arrays. In this regard, convolutional embedding layers can be used in network heads in the presence of several sensor records. HyDRA presents several opportunities for future research and development by considering different damage diagnosis setups and embedding more advanced neural architectures. The concept of attention can be integrated within the recurrent modules for more effective learning.

References

Abdeljaber, O., Avci, O., Kiranyaz, M. S., Boashash, B., Sodano, H., and Inman, D. J. (2018). "1-D CNNs for structural damage detection: Verification on a structural health monitoring benchmark data." Neurocomputing, 275, 1308-1317.

AES (2018). "AES recommended practice for professional digital audio - Preferred sampling frequencies for applications employing pulse-code modulation." Audio Engineering Society, New York, USA.

Akkar, S., and Özen, Ö. (2005). "Effect of peak ground velocity on deformation demands for SDOF systems." Earthquake engineering & structural dynamics, 34(13), 1551-1571.

Ancheta, T. D., Darragh, R. B., Stewart, J. P., Seyhan, E., Silva, W. J., Chiou, B. S.-J., Wooddell, K. E., Graves, R. W., Kottke, A. R., Boore, D. M., Kishida, T., and Donahue, J. L. (2014). "NGA-West2 Database." Earthquake Spectra, 30(3), 989-1005.

ASCE (2021). "2021 Report Card for America's Infrastructure."

ATC (Applied Technology Council) (2012). Seismic performance assessment of buildings, prepared for federal emergency management agency. FEMA-P58. Washington, DC: ATC.

Avci, O., Abdeljaber, O., Kiranyaz, S., Hussein, M., Gabbouj, M., and Inman, D. J. (2021). "A review of vibration-based damage detection in civil structures: From traditional methods to Machine Learning and Deep Learning applications." Mechanical systems and signal processing, 147, 107077.

Azimi, M., and Pekcan, G. (2020). "Structural health monitoring using extremely compressed data through deep learning." Computer-Aided Civil and Infrastructure Engineering, 35(6), 597-614.

Baker, J. W. (2015). "Efficient analytical fragility function fitting using dynamic structural analysis." Earthquake Spectra, 31(1), 579-599.

Balsamo, L., Betti, R., and Beigi, H. (2014). "A structural health monitoring strategy using cepstral features." Journal of Sound and Vibration, 333(19), 4526-4542.

Bogert, B. P., Healy, M. J. R., and Tukey, J. W. "The quefrency alanysis of time series for echoes; Cepstrum, pseudo-autocovariance, cross-cepstrum and saphe cracking." Proc., Time series analysis, Wiley, 209-243.

Campbell, K. W., and Bozorgnia, Y. (2014). "NGA-West2 Ground Motion Model for the Average Horizontal Components of PGA, PGV, and 5% Damped Linear Acceleration Response Spectra." Earthquake Spectra, 30(3), 1087-1115.

CESMD (2021). "Center for Engineering Strong Motion Data." <https://www.strongmotioncenter.org/>.

Chan, W., Jaitly, N., Le, Q., and Vinyals, O. "Listen, attend and spell: A neural network for large vocabulary conversational speech recognition." Proc., 2016 IEEE International Conference on Acoustics, Speech and Signal Processing (ICASSP), IEEE, 4960-4964.

Chen, T., and Guestrin, C. "Xgboost: A scalable tree boosting system." Proc., Proceedings of the 22nd acm sigkdd international conference on knowledge discovery and data mining, 785-794.

Cho, K., Van Merriënboer, B., Gulcehre, C., Bahdanau, D., Bougares, F., Schwenk, H., and Bengio, Y. (2014). "Learning phrase representations using RNN encoder-decoder for statistical machine translation." arXiv preprint arXiv:1406.1078.

Chollet, F., and Others (2015). "Keras." <https://github.com/keras-team/keras>.

Civera, M., Ferraris, M., Ceravolo, R., Surace, C., and Betti, R. (2019). "The Teager-Kaiser energy cepstral coefficients as an effective structural health monitoring tool." Applied Sciences, 9(23), 5064.

Cornell, C., and Krawinkler, H. (2000). "Progress and challenges in seismic performance assesment." PEER Center News, 1-3.

Dackermann, U., Smith, W. A., and Randall, R. B. (2014). "Damage identification based on response-only measurements using cepstrum analysis and artificial neural networks." Structural Health Monitoring, 13(4), 430-444.

Davis, S., and Mermelstein, P. (1980). "Comparison of parametric representations for monosyllabic word recognition in continuously spoken sentences." IEEE transactions on acoustics, speech, signal processing, 28(4), 357-366.

Davis, S., and Mermelstein, P. (1980). "Comparison of parametric representations for monosyllabic word recognition in continuously spoken sentences." IEEE Transactions on Acoustics, Speech, and Signal Processing, 28(4), 357-366.

Dutta, A. (1999). On energy-based seismic analysis and design of highway bridges, State University of New York at Buffalo.

Eltouny, K. A., and Liang, X. (2021). " Bayesian-optimized unsupervised learning approach for structural damage detection." Computer-Aided Civil and Infrastructure Engineering, 36(10), 1249-1269.

Eltouny, K. A., and Liang, X. (2022). " Large-scale structural health monitoring using composite recurrent neural networks and grid environments." Computer-Aided Civil and Infrastructure Engineering.

Ferraris, M., Civera, M., Ceravolo, R., Surace, C., and Betti, R. "Using enhanced cepstral analysis for structural health monitoring." Proc., Proceedings of the 13th International Conference on Damage Assessment of Structures, Springer, 150-165.

Gal, Y., and Ghahramani, Z. "Dropout as a bayesian approximation: Representing model uncertainty in deep learning." Proc., international conference on machine learning, 1050-1059.

Guan, X., Burton, H., Shokrabadi, M., and Yi, Z. (2021). "Seismic Drift Demand Estimation for Steel Moment Frame Buildings: From Mechanics-Based to Data-Driven Models." Journal of Structural Engineering, 147(6), 04021058.

Haddadi, H., Shakal, A., Huang, M., Parrish, J., Stephens, C., Savage, W., and Leith, W. "Report on progress at the center for engineering strong motion data (CESMD)." Proc., Proc. World Conf. Earthq. Eng., Lisbon, 1-7.

Hamburger, R., Rojahn, C., Heintz, J., and Mahoney, M. "FEMA P58: Next-generation building seismic performance assessment methodology." Proc., 15th world conference on earthquake engineering.

Kaviani, P., Zareian, F., and Taciroglu, E. (2014). "Performance-Based Seismic Assessment of Skewed Bridges, Report PEER 2014/01." Pacific Earthquake Engineering Research Center, University of California Irvine.

Khodabandehlou, H., Pekcan, G., and Fadali, M. S. (2019). "Vibration-based structural condition assessment using convolution neural networks." Structural Control and Health Monitoring, 26(2), e2308.

Küçükdogan, B. (2007). "Investigation of the effect of ground-motion intensity measures on seismic demand parameters using probabilistic methods." Department of Civil Engineering, Middle East Technical University.

Liang, X. (2019). " Image-based post-disaster inspection of reinforced concrete bridge systems using deep learning with Bayesian optimization." Computer-Aided Civil and Infrastructure Engineering, 34(5), 415-430.

Liang, X., and Mosalam, K. M. (2020). "Ground motion selection and modification evaluation for highway bridges subjected to Bi-directional horizontal excitation." Soil Dynamics and Earthquake Engineering, 130, 105994.

Liang, X., Mosalam, K.M., and Günay, S. (2016). "Direct Integration Algorithms for Efficient Nonlinear Seismic Response of Reinforced Concrete Highway Bridges." Journal of Bridge Engineering, 21(7), 04016041.

Liang, X., Mosalam, K.M., and Muin, S. (2018) "Simulation-based data-driven damage detection for highway bridge systems." In 11th National conference on earthquake engineering.

Mangalathu, S., and Jeon, J.-S. (2020). "Ground Motion-Dependent Rapid Damage Assessment of Structures Based on Wavelet Transform and Image Analysis Techniques." Journal of Structural Engineering, 146(11), 04020230.

McKenna, F., Scott, M. H., and Fenves, G. L. (2010). "Nonlinear finite-element analysis software architecture using object composition." Journal of Computing in Civil Engineering, 24(1), 95-107.

Mei, Q., Gül, M., and Boay, M. (2019). "Indirect health monitoring of bridges using Mel-frequency cepstral coefficients and principal component analysis." Mechanical Systems and Signal Processing, 119, 523-546.

Muin, S., Chern, C., and Mosalam, K. "Human-machine collaboration framework for brdige health monitoring." Proc., SMIP20 Seminar on utilization of strong-motion data, 100-127.

Oppenheim, A. V., and Schafer, R. W. (2004). "From frequency to quefrency: A history of the cepstrum." IEEE signal processing Magazine, 21(5), 95-106.

Riddell, R. (2007). "On ground motion intensity indices." Earthquake Spectra, 23(1), 147-173.

Sajedi, S., and Liang, X. (2021a). " Uncertainty-assisted deep vision structural health monitoring." Computer‐Aided Civil and Infrastructure Engineering, 36(2), 126-142.

Sajedi, S., and Liang, X. (2021b). "Dual Bayesian inference for risk-informed vibration-based damage diagnosis." Computer-Aided Civil and Infrastructure Engineering, 36(9), 1168-1184.

Sajedi, S. O., and Liang, X. (2020a). "A data-driven framework for near real-time and robust damage diagnosis of building structures." Structural Control and Health Monitoring, 27(3), e2488.

Sajedi, S. O., and Liang, X. (2020b). "Vibration-based semantic damage segmentation for large-scale structural health monitoring." Computer-Aided Civil and Infrastructure Engineering, 35(6), 579-596.

Sajedi, S. O., Liu, W., Eltouny, K. A., Behdad, S., Zheng, M., and Liang, X. (2022). " Uncertainty-Assisted Image-Processing for Human-Robot Close Collaboration." IEEE Robotics and Automation Letters, 7(2), 4236-4243.

Tamhidi, A., Kuehn, N., Ghahari, S. F., Rodgers, A. J., Kohler, M. D., Taciroglu, E., and Bozorgnia, Y. (2021). "Conditioned Simulation of Ground-Motion Time Series at

Uninstrumented Sites Using Gaussian Process Regression." Bulletin of the Seismological Society of America.

Virtanen, P., Gommers, R., Oliphant, T. E., Haberland, M., Reddy, T., Cournapeau, D., Burovski, E., Peterson, P., Weckesser, W., and Bright, J. (2020). "SciPy 1.0: fundamental algorithms for scientific computing in Python." Nature methods, 17(3), 261-272.

Xu, Y., Lu, X., Cetiner, B., and Taciroglu, E. (2021). "Real-time regional seismic damage assessment framework based on long short-term memory neural network." Computer-Aided Civil and Infrastructure Engineering, 36(4), 504-521.